Improving Satellite Quantitative Precipitation Estimation Using GOES-Retrieved Cloud Optical Depth

RONALD STENZ, XIQUAN DONG, AND BAIKE XI

Department of Atmospheric Sciences, University of North Dakota, Grand Forks, North Dakota

ZHE FENG

Pacific Northwest National Laboratory, Richland, Washington

ROBERT J. KULIGOWSKI

NOAA/NESDIS/Center for Satellite Applications and Research, College Park, Maryland

(Manuscript received 15 April 2015, in final form 2 October 2015)

ABSTRACT

To address gaps in ground-based radar coverage and rain gauge networks in the United States, geostationary satellite quantitative precipitation estimation (QPE) such as the Self-Calibrating Multivariate Precipitation Retrieval (SCaMPR) can be used to fill in both spatial and temporal gaps of ground-based measurements. Additionally, with the launch of Geostationary Operational Environmental Satellite R series (GOES-R), the temporal resolution of satellite QPEs may be comparable to Weather Surveillance Radar-1988 Doppler (WSR-88D) volume scans as GOES images will be available every 5 min. However, while satellite QPEs have strengths in spatial coverage and temporal resolution, they face limitations, particularly during convective events. Deep convective systems (DCSs) have large cloud shields with similar brightness temperatures (BTs) over nearly the entire system, but widely varying precipitation rates beneath these clouds. Geostationary satellite QPEs relying on the indirect relationship between BTs and precipitation rates often suffer from large errors because anvil regions (little or no precipitation) cannot be distinguished from rain cores (heavy precipitation) using only BTs. However, a combination of BTs and optical depth τ has been found to reduce overestimates of precipitation in anvil regions. A new rain mask algorithm incorporating both τ and BTs has been developed, and its application to the existing SCaMPR algorithm was evaluated. The performance of the modified SCaMPR was evaluated using traditional skill scores and a more detailed analysis of performance in individual DCS components by utilizing the Feng et al. classification algorithm. SCaMPR estimates with the new rain mask benefited from significantly reduced overestimates of precipitation in anvil regions and overall improvements in skill scores.

1. Introduction

Satellite quantitative precipitation estimation (QPE) is valuable to the National Oceanic and Atmospheric Administration (NOAA)/National Weather Service (NWS) for flood and river forecasts (Zhang and Qi 2010; Zhang et al. 2011). Geostationary satellite QPEs such as the Self-Calibrating Multivariate Precipitation Retrieval (SCaMPR) can provide continuous spatial coverage (Scofield and Kuligowski 2003) to fill in the gaps from both surface rain gauge network measurements and radar QPEs because of their limited spatial coverages (Krajewski and Smith 2002; Maddox et al. 2002). While numerous geostationary satellite QPEs exist (Negri and Adler 1981; Adler and Negri 1988; Vicente et al. 1998; Scofield and Kuligowski 2003; Kuligowski 2010), this study will focus on SCaMPR (Kuligowski 2010), an infrared (IR) brightness temperature (BT)-based algorithm being developed in preparation for the Geostationary Operational Environmental Satellite R series (GOES-R) launch by NOAA/NESDIS.

Similar to other IR-based algorithms, SCaMPR faces limitations arising from the weak relationship between

Corresponding author address: Dr. Xiquan Dong, Department of Atmospheric Sciences, University of North Dakota, 4149 University Ave., Stop 9006, Grand Forks, ND 58203-9006.
E-mail: dong@aero.und.edu

DOI: 10.1175/JHM-D-15-0057.1

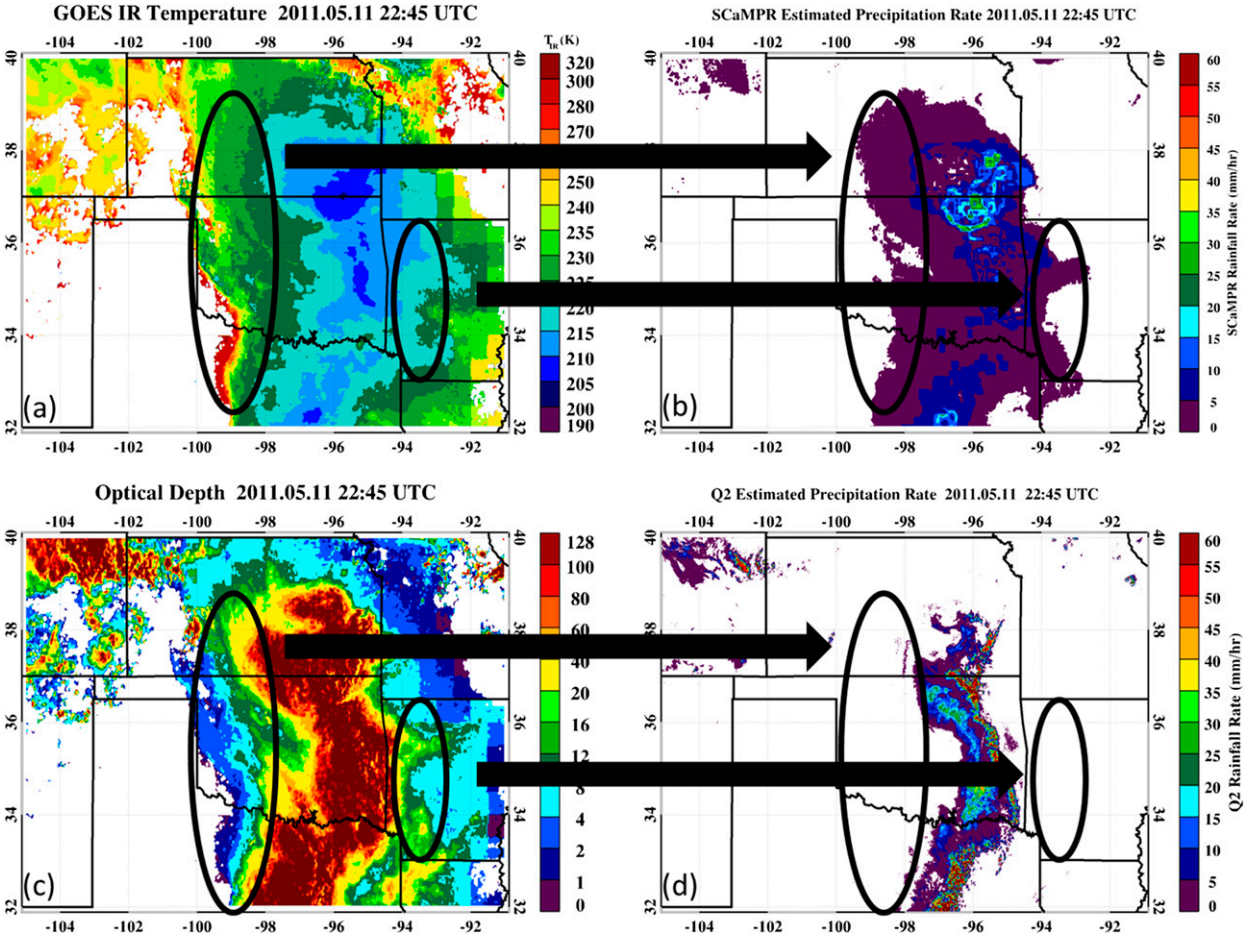

FIG. 1. (a) GOES IR temperature (K), (b) SCaMPR-estimated precipitation rate (mm h^{-1}), (c) GOES-retrieved cloud optical depth, and (d) Q2 precipitation rate (mm h^{-1}) at 2245 UTC 11 May 2011. Each oval indicates regions with cold BTs but optically thin clouds where SCaMPR estimated precipitation that was not observed by radar.

BTs and surface precipitation. For example, the BTs of anvil clouds from deep convection are similar to those of the parent precipitating clouds (Feng et al. 2011, 2012). More effective separation of anvil clouds from deep convective clouds can improve the performance of IR-based satellite QPEs (Vicente et al. 1998). A rain mask using a combination of BTs and cloud optical depth τ has been developed (Stenz et al. 2014), which can reduce overestimates of precipitation in anvil regions of deep convective systems (DCSs), providing more accurate geostationary satellite QPEs (Stenz et al. 2014). Because rain cores of DCSs are located where clouds are thicker than the surrounding anvil cloud shield, inclusion of optical depth in satellite QPE algorithms can aid in separating these two regions with drastically different precipitation rates but similar BTs (Stenz et al. 2014). An example of the schematic diagram used for the Stenz et al. (2014) algorithm, and the algorithm discussed in this paper, is shown in Fig. 1. The observed precipitating area (Fig. 1d) is more closely related to the cloud optical depth (Fig. 1c) than the cloud-top temperature (Fig. 1a). As a result, the use of only brightness temperatures to estimate precipitation rates (Fig. 1b) leads to large overestimates of precipitating area. In the encircled regions, cold BTs are present but cloud optical thickness is relatively low. These are regions where the inclusion of optical depth into a BT-based precipitation estimation algorithm such as SCaMPR will reduce the overestimates of precipitating area shown in Fig. 1.

In this study, the performance of the SCaMPR algorithm and SCaMPR with an optical-depth-based rain mask applied to it (SCaMPR-OD) will be evaluated against high-quality multiradar-based precipitation estimates, next-generation QPE (Q2), for three warm seasons (2010–12) over the southern Great Plains (SGP). Ground-based radar data have been used in recent studies (Kirstetter et al. 2012; Amitai et al. 2012) to validate satellite QPEs, such as those from TRMM. In

this study, a pixel-level optical-depth-based rain mask algorithm has been developed and applied to SCaMPR, and improvements in the estimated precipitating area and volume have been documented. This algorithm is based on the schematic diagram of the Stenz et al. (2014) algorithm but is more computationally efficient and more physically based rather than empirically based. For example, the computational time using the new algorithm was reduced by 20%–30% compared to the Stenz et al. (2014) method based on test runs over the 8° × 14° study domain. Similar computational time savings are expected to extend to the larger domain for the complete version of SCaMPR. Additionally, while the Stenz et al. (2014) algorithm utilized brightness temperature thresholds to create a radius of influence around identified optical depth cores (similar in idea to the Steiner radar-based classification of convective and stratiform regions; Steiner et al. 1995), the algorithm discussed in this paper functions at the pixel level and does not use any radii of influence. This approach removes subjective criteria for radii of influence, while also eliminating potential biases possible using the Stenz et al. (2014) algorithm for storms with asymmetrical precipitation regions. For example, in a sheared environment the Stenz et al. (2014) algorithm may be prone to overestimating precipitation in upshear regions because the precipitating area is determined with a radius of influence from regions of high optical depth and cold brightness temperatures. Typically, upshear regions have less precipitation and the transition to nonprecipitating optically thin clouds occurs more quickly than in downshear regions. In these instances, the Stenz et al. (2014) algorithm may identify regions upshear of convective cores as precipitating even if these regions are nonprecipitating and have low optical depth values. The new pixel-based approach, which does not rely on a radius of influence, is directly based on the satellite pixel-retrieved properties and will not suffer from the potential upshear bias that could occur with the Stenz et al. (2014) algorithm. While the new algorithm does have an empirical component—the chosen optical depth threshold to be used—it eliminates the need to empirically choose radii of influence, along with brightness temperature and optical depth thresholds that are matched with an empirically or subjectively determined radius of influence.

Improvement of satellite QPEs in DCSs is important because the majority of flash flooding events in the United States arise from DCSs, and a large portion of warm season total rainfall is produced by these systems. As near-real-time satellite QPEs can aid in both regional and global disaster preparedness and mitigation, improvement of these products can protect lives and property (Hong et al. 2007). To improve the well-documented problem of overestimates in anvil regions from IR-based satellite QPEs during convection (Stenz et al. 2014), a new pixel-level optical-depth-based rain mask will be applied to SCaMPR and thoroughly evaluated against Q2. Section 2 of this paper will briefly introduce the datasets used for precipitation retrieval and evaluation, while section 3 describes the derivation of the rain mask from optical depth retrievals. The impact of this mask on the accuracy of the rainfall retrievals is discussed in sections 4 and 5, followed by concluding comments in section 6 on more general applications of this optical-depth-based rain mask and its limitations.

2. Data

a. *Q2 data*

National Mosaic and Multi-Sensor QPE (NMQ) Q2 during warm season convective events from 2010 to 2012 has been collected for this study for NMQ tile 6, which has northern and southern boundaries at 40° and 20°N and is bounded longitudinally by 110° and 90°W. NMQ Q2 provides multiradar precipitation estimates with a grid resolution of 1 km × 1 km (http://www.nssl.noaa.gov/projects/q2/q2.php). Q2 is produced using quality-controlled radar reflectivity data from multiple radars to automatically classify precipitation as convective rain, stratiform rain, warm rain, hail, and snow (Zhang et al. 2011). These classifications assign reflectivity–rain rate (Z–R) relationships to each pixel to provide the Q2 rain rates (Zhang et al. 2011). These Q2 have been found to be consistent with Oklahoma Mesonet rain gauge network observations for both precipitation amounts and characteristics (Stenz et al. 2014).

b. *SCaMPR*

SCaMPR, the GOES-R algorithm for the estimation and detection of rainfall, attempts to combine the strengths of microwave-estimated rain rates with the better spatial and temporal coverage of GOES data by calibrating predictors from GOES IR BTs against microwave-estimated rainfall rates (Kuligowski 2010). Brightness temperature differences between GOES bands are used to determine three cloud types. Separately matched datasets for these three cloud types (water, ice, and cold-top convective) and four latitude bands are updated when new microwave-estimated rain rates are available. Each time the matched datasets are updated, discriminant analysis is used to identify the two best predictors and coefficients for discriminating raining from nonraining pixels; stepwise forward linear regression is used to select the two best predictors and

coefficients for deriving rain rates (Kuligowski 2010). The predictors available for this version of SCaMPR were GOES bands 3 (6.7 μm) and 4 (10.7 μm), the difference between these two bands, and two measures of local texture from the GOES band 4 field. The nonlinear relationship between rain rates and IR brightness temperatures is accounted for by regressing IR brightness temperatures against rain rates in log–log space to generate additional rain-rate predictors. Lookup tables restore retrieved rain rates to the correct distribution by matching the regression-derived cumulative distribution functions (CDFs) of rain rates to the CDFs of microwave-estimated rain rates.

c. *Hybrid classification*

DCSs over the study region are objectively identified and subsequently partitioned into convective cores, stratiform rain regions, and anvil regions through analysis of collocated ground-based radar and geostationary satellite data (Feng et al. 2011). The detailed classification of DCS components provided by this hybrid classification allows the performance of SCaMPR and SCaMPR-OD to be evaluated in specific regions of DCSs. The radar-identified convective core (CC) region is characterized by high reflectivity values using the convective–stratiform algorithm originally developed in Steiner et al. (1995) and modified by Feng et al. (2011). For this study, the threshold for a pixel to be identified as a CC was set to 45 dBZ. Radar-identified stratiform (SR) regions account for precipitation echoes that fall below the convective reflectivity threshold (Steiner et al. 1995). Anvil cloud (AC) regions are partially identified by radar, where larger echo returns (>0 dBZ) are detectable by radar with echo bases above 6 km. However, limited power returns from anvil regions frequently make these clouds undetectable by ground-based precipitation radars such as the Weather Surveillance Radar-1988 Doppler (WSR-88D; Stenz et al. 2014). Since GOES can view the entire cloud shield, GOES data are used to supplement WSR-88D data to identify thin anvil regions of DCSs. In this study, the hybrid classification product is produced at a grid resolution of 4 km × 4 km, and with the same temporal resolution as SCaMPR and Q2 instantaneous estimates for comparison. The radar reflectivity data used in the classification are on a 1 km × 1 km grid, so the radar classified DCS components are averaged to a 4 km × 4 km grid by selecting the most frequent classification within the 4 km × 4 km grid box.

d. *Cloud optical depth retrievals*

GOES-retrieved cloud optical depth used for the rain mask in this study was provided by NASA's Langley Research Center. These retrievals were generated using the Visible Infrared Solar-Infrared Split Window Technique (VISST) algorithm (Minnis et al. 2008; http://www-pm.larc.nasa.gov/satimage/visst.html). Optical depth is retrieved by matching parameterizations of theoretical radiance calculations for water droplet and ice crystal size distributions to measurements. Parameterizations for seven water and nine ice crystal size distributions are used in this retrieval, along with observed radiances from the 0.65, 3.9, 10.8, and 12.0 μm channels. Other required inputs in this optical depth retrieval include atmospheric profiles from in situ measurements or model data, surface characterization from the International Geosphere–Biosphere Programme (IGBP), clear sky radiances from Clouds and the Earth's Radiant Energy System (CERES), and 4-km-resolution data from GOES. Additionally, narrowband to broadband flux conversion functions are required in this algorithm. The optical depth retrievals used in this study cover 32°–40°N and 105°–91°W over the SGP region. Only retrievals during daylight hours were used, as the solar zenith angles during dawn and dusk often produce large errors in the radiance calculations that affect accurate optical depth retrievals.

e. *Data processing*

To allow direct comparisons between all datasets, each dataset has been regridded to the same 4 km × 4 km grid at a 30-min temporal resolution matching the GOES images. For the Q2 data, the 1 km × 1 km estimates are averaged onto a 4 km × 4 km grid to match the resolution of the satellite data. Both the SCaMPR and optical depth retrieval data are matched to the 4 km × 4 km grid of the hybrid classification output using nearest grid matching. No temporal adjustments to the data were needed, as the Q2 instantaneous estimates and hybrid classification product were available at the same times as the GOES images.

3. Methodology

The precipitation estimates from SCaMPR and SCaMPR-OD were compared to Q2 for both overall statistics and statistics for each DCS region. Application of the rain mask is performed in one step, where all SCaMPR pixels with estimated rain rates >0 mm h^{-1} are set to zero for pixels identified as nonprecipitating by the rain mask. A pixel is identified as nonprecipitating by the rain mask if the retrieved optical depth of the pixel is less than the prescribed threshold value. Results from SCaMPR and SCaMPR-OD are directly compared with Q2 on a 4 km × 4 km grid.

In this study, days with convective activity within the SGP study region bounded by 32° and 40°N and 105° and

91°W from the warm seasons from 2010 to 2012 were used for analysis. The analysis was performed for every GOES image that temporally coincided with the hybrid classification and Q2 datasets. The warm season for this study is defined as April–September, consistent with previous studies (Wu et al. 2012; Stenz et al. 2014). As shown in Fig. 2, a total of 128 different optical depth thresholds were applied to SCaMPR to investigate how the performance of SCaMPR-OD varies with the chosen cloud optical depth threshold. Critical success index (CSI) is used to determine the optimal optical depth value for the rain mask to detect measureable precipitation (rates $>0.25\,\mathrm{mm\,h^{-1}}$):

$$\mathrm{CSI} = H/(H + M + F), \tag{1}$$

where H represents the number of hits (estimate and observation of measurable precipitation), M represents the number of misses (measurable precipitation was observed but not estimated), and F represents the number of false alarms (measurable precipitation was estimated but not observed). The purpose of the rain mask is simply to aid in producing the most accurate estimates of the instantaneous precipitating area from a given GOES image; thus, the skill of SCaMPR-OD in detecting measurable precipitation provides an objective means of determining improvement compared to the original SCaMPR estimates. This skill was also evaluated over the anvil and thin anvil/unclassified regions where the bulk of modifications to SCaMPR occur, to ensure that skill is also improved in these regions in addition to the overall SCaMPR estimates. In addition to evaluating the CSI of SCaMPR and SCaMPR-OD, the Heidke skill score (HSS) for SCaMPR and SCaMPR-OD was examined:

$$\mathrm{HSS} = 2(HN - FM)/[(H + M)(M + N) + (H + F)(F + N)], \tag{2}$$

where N represents null occurrences (measurable precipitation was neither estimated nor observed). As the HSS accounts for a chance forecast (estimate) being correct, it provides another means to validate the improvements of SCaMPR-OD over SCaMPR. While the CSI and HSS were calculated for the anvil and thin anvil/unclassified regions, these scores are not possible to calculate for CC and SR regions. By definition CC and SR regions have measurable precipitation; therefore, no false alarms in Eqs. (1) and (2) are possible, which prevents the fair use of CSI and HSS to determine skill in CC and SR regions.

The total estimated precipitating area and total estimated precipitation was also calculated from both Q2

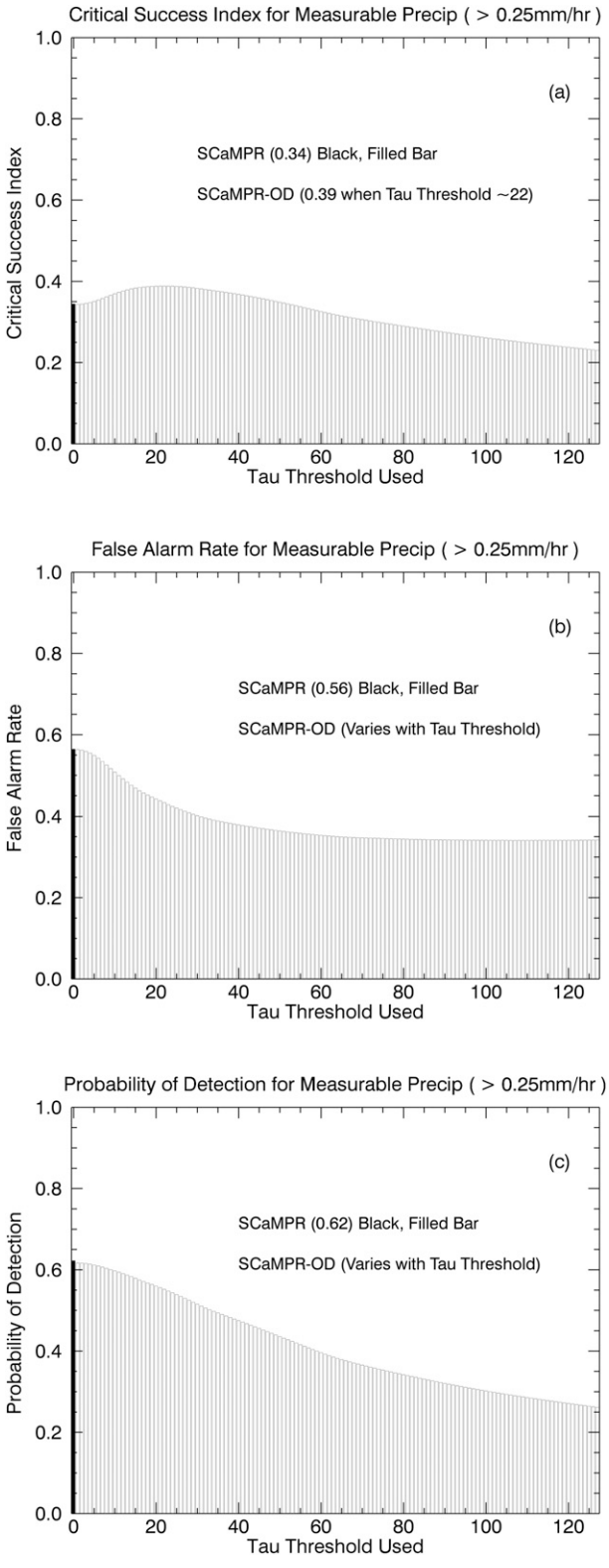

FIG. 2. (a) CSI, (b) FAR, and (c) POD for SCaMPR (black, filled bar) and SCaMPR-OD (empty bars) for measurable precipitation over the SGP region during warm season convective events from 2010 through 2012.

and SCaMPR. By calculating the total estimated precipitating area, SCaMPR with and without the rain mask applied could be examined to determine how well they represent the actual size of the precipitating regions of DCSs, using Q2 as ground truth. The total estimated precipitation comparison can aid in studying how well the performance of SCaMPR is in estimating the overall water budget of DCSs. As the bias of Q2 is known from previous studies (Chen et al. 2013; Stenz et al. 2014; Zhang et al. 2014), the performance of SCaMPR with and without the rain mask in accurately representing total rainfall from DCSs can be assessed.

Additionally, the distribution of estimated precipitation among DCS components was calculated for Q2 and SCaMPR with and without the rain mask applied. As Q2 provides a reasonable estimate for the actual distribution of precipitation among DCS components (Stenz et al. 2014), these were treated as ground truth for this evaluation. Comparison of the estimated precipitation distributions from SCaMPR to the Q2 precipitation distributions provides insight into how well SCaMPR represents the precipitation variations across a DCS. Additionally, the improvements made to this representation by use of rain masks can be quantitatively evaluated. Potential biases in estimated rainfall rates in specific regions of DCSs can also be identified.

The combination of analyses of skill scores in precipitation detection, estimated precipitation distributions, estimated precipitating area, and estimated total precipitation will provide a detailed quantitative analysis of the performance of SCaMPR during DCSs. Additionally, these analyses will provide more insight into the improvement from adding a rain mask to SCaMPR and how much the application of a rain mask can reduce significant overestimates of precipitation from SCaMPR that have been identified during warm season convection (Stenz et al. 2014).

4. Results

Application of the optical-depth-based rain mask improved the CSI for estimated precipitation over a broad range of optical depth thresholds (Fig. 2a). The CSI from SCaMPR-OD increased with increasing optical depth thresholds up to a maximum of 0.39 with an optical depth threshold of 22, surpassing the CSI of the original version of SCaMPR by 0.05, then gradually decreased as the optical depth threshold was increased beyond 22 (Fig. 2a). The increase in CSI is attributed to an initial rapid reduction in false alarm rate (FAR) as the optical depth threshold of the rain mask was increased (Fig. 2b), while the probability of detection (POD) decreases more slowly (Fig. 2c). Once the optical depth thresholds exceed ~50, reductions in FAR are insignificant (Fig. 2b), while POD continues to decrease (Fig. 2c), resulting in a lower CSI than the original SCaMPR.

For only anvil and thin anvil/unclassified regions, the CSI from SCaMPR-OD was also greater than that of the original version of SCaMPR (Fig. 3a). However, this increase occurs over a narrower range (τ threshold less than ~30) and the optimal threshold for CSI in these regions is ~15. Again, the increase in CSI occurs from a more rapid reduction in FAR (Fig. 3b) than the decrease in POD (Fig. 3c). Once the optical depth threshold used approaches ~30 for anvil and thin anvil/unclassified regions, reductions in POD (Fig. 3c) outweigh those in FAR (Fig. 3b), reducing CSI compared to the original SCaMPR.

Calculation of the HSS for SCaMPR and SCaMPR-OD (Fig. 4) produces similar results to those of the calculated CSI. SCaMPR-OD has a broad region (τ threshold less than ~60) with an improved HSS over the original SCaMPR (Fig. 4). The HSS is maximized for SCaMPR-OD when an optical depth threshold of ~25 is used. Figure 5 shows the HSS calculated for only the anvil and thin anvil/unclassified regions for SCaMPR and SCaMPR-OD. Again, these results are similar to those of the CSI with SCaMPR-OD showing improvements over SCaMPR in a narrower range, with the optimal optical depth threshold for only anvil and thin anvil/unclassified regions being lower than that for all regions (Fig. 5).

Figure 6 shows the total estimated precipitating areas from SCaMPR, SCaMPR-OD, and Q2 over the entire study region for the duration of the study. The total estimated precipitating area is calculated by summing the precipitating areas from each instantaneous estimate for the duration of the study. As demonstrated in Fig. 6, the total estimated precipitating area for SCaMPR-OD decreases as the optical depth threshold increases, matching the Q2 precipitating area when an optical depth threshold of 22 is used. This result is consistent with Fig. 2, where the maximum CSI occurs with an optical depth threshold of 22. Compared to the Q2 precipitating area, the original version of SCaMPR overestimates the precipitating area by 45.5%. The causes of the reduction in precipitating area with the rain mask applied are shown in Fig. 7. Compared to the classified Q2 precipitating area, both CC and SR precipitating areas from SCaMPR and SCaMPR-OD are underestimated (Figs. 7a,b), but the precipitating areas of anvil and thin anvil/unclassified regions are greatly overestimated. As illustrated in Figs. 7c and 7d, increasing the optical depth threshold in SCaMPR-OD reduces the overestimates of precipitating area for anvil

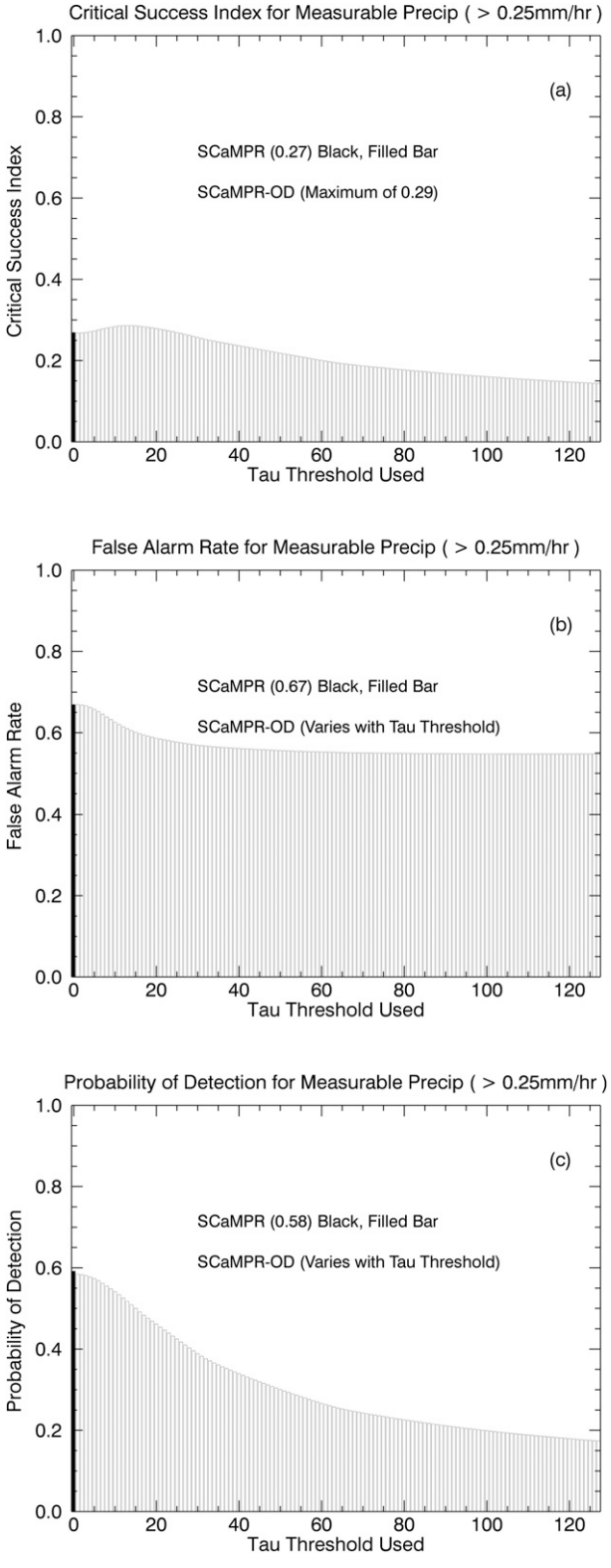

FIG. 3. As in Fig. 2, but for anvil and thin anvil/unclassified regions only.

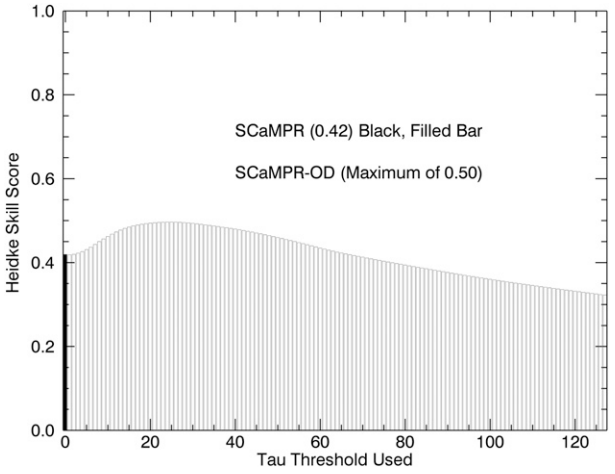

FIG. 4. The HSS for measurable precipitation for SCaMPR (black, filled bar) and SCaMPR-OD (empty bars) over the SGP region during warm season convective events from 2010 through 2012.

and thin anvil/unclassified regions dramatically. For example, using the skill-maximizing optical depth threshold of 22 reduces overestimates of precipitating area in anvil regions by 51.2% (overestimate of 112.8% becomes an overestimate of 61.6%; Fig. 7c) and by 216.4% (overestimate of 369.7% becomes an overestimate of 153.3%) in thin anvil/unclassified regions (Fig. 7d). Slight reductions in estimated precipitating area for CC (Fig. 7a) and SR (Fig. 7b) regions also occur when the skill-maximizing optical depth threshold is used. These slight reductions possibly result from potential shifting of the optical depth retrievals during the regridding process or may occur because of the averaging from a 1 km × 1 km to a 4 km × 4 km grid. Both of these uncertainties will be discussed in greater detail in the discussion section. These increases in underestimates of precipitating area for CC and SR regions are consistent with the decreases in POD for SCaMPR-OD in Fig. 2c.

Figures 8 and 9 illustrate the improvements in precipitating area from SCaMPR to SCaMPR-OD when compared to Q2. Both figures show instantaneous rain-rate estimates from SCaMPR (Figs. 8a, 9a), SCaMPR-OD using an optical depth threshold of 22 (Figs. 8b, 9b), and Q2 (Figs. 8c, 9c) at the same time. For the 11 May 2011 case in Fig. 8, the estimated precipitating area from SCaMPR-OD has been compared to the original SCaMPR estimates, with much of this reduction over western Arkansas and central Oklahoma where no precipitation was observed by radar. During the 20 May 2011 case, application of the rain mask significantly reduces estimated precipitating area over central Oklahoma, producing SCaMPR-OD

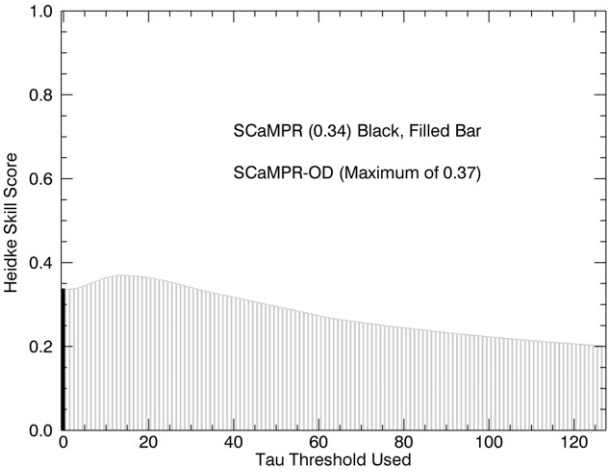

FIG. 5. As in Fig. 4, but for anvil and thin anvil/unclassified regions only.

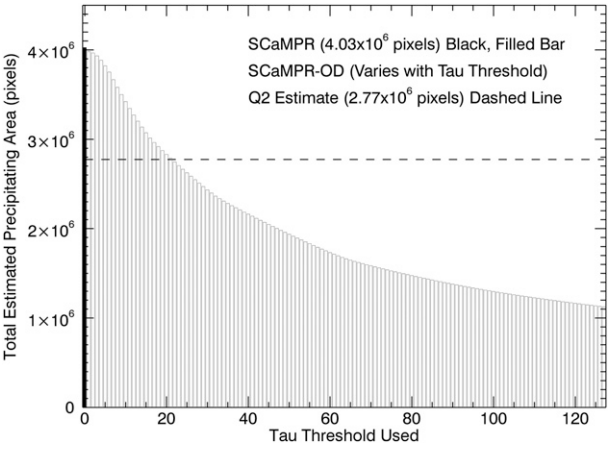

FIG. 6. Total estimated precipitating areas from SCaMPR (black, filled bar), SCaMPR-OD (empty bars), and Q2 (dashed line) over the SGP region.

estimates more consistent with the radar observations than the original SCaMPR estimates. In both of these cases, overestimates of precipitating area still exist after application of the rain mask, but the radar-observed precipitation is well captured in the SCaMPR estimates.

The total estimated amount of precipitation from SCaMPR, SCaMPR-OD, and Q2 over the entire study region for the duration of the study is shown in Fig. 10. Compared to the baseline of Q2, SCaMPR has a wet bias of 83.4%, while the wet bias for SCaMPR-OD decreases as the optical depth threshold increases, reaching no bias with an optical depth threshold of ~62. At the CSI-maximizing optical depth threshold of 22, SCaMPR-OD reduces the wet bias of SCaMPR by 40.5%. Figure 11 shows the total amount of estimated precipitation in CC, SR, AC, and unclassified regions of DCSs. This differs from Fig. 7 because the summation of all estimated precipitation in each region is being shown in Fig. 11 rather than the estimated total precipitating area for each region. The total amount of precipitation in CC regions is significantly underestimated by all versions of SCaMPR, while large overestimates occur for SR regions (Figs. 11a,b); this is expected as the IR temperature distributions in these two regions are virtually indistinguishable [refer to Fig. 5 of Feng et al. (2011)], and therefore, IR-based satellite precipitation retrieval has low skill in distinguishing actual locations of heavier precipitation cores. For anvil and thin anvil/unclassified regions, the original SCaMPR overestimates precipitation by an order of magnitude compared to Q2 (Figs. 11c,d). Application of the rain mask dramatically reduces overestimates in both of these regions, but large overestimates still exist.

The estimated precipitation distribution among rain-core (CC and SR) and non-rain-core (AC and thin anvil/unclassified) regions for all versions of SCaMPR shows a strong wet bias in non-rain-core regions and a strong dry bias in rain-core regions (Fig. 12). While nearly 93% of Q2 precipitation occurs in rain-core regions, SCaMPR estimates only show ~46% of precipitation in rain-core regions (Fig. 12). Application of the rain mask improves the SCaMPR-estimated precipitation distribution as the optical depth threshold is increased (Fig. 12). For the skill-maximizing optical depth threshold of 22, the majority of SCaMPR-estimated precipitation now occurs in rain-core regions (54.9%) but the large wet bias for non-rain-core regions is still present (45.1% still in non-rain-core regions; Fig. 12b).

5. Discussion

Applying an optical-depth-based rain mask to SCaMPR estimates increased skill (CSI and HSS) in the detection of precipitation and improved estimates of precipitating areas, amounts, and precipitation distributions between rain-core and non-rain-core regions. Optical depth thresholds less than 50 produce improved skill (CSI and HSS) compared to the original SCaMPR, with CSI being maximized when an optical depth threshold of 22 was chosen. While the optical depth threshold of 22 works best for the entire study period, for exceptionally well-organized convective systems such as those on 11 and 20 May 2011, more stringent optical depth thresholds can increase the performance of SCaMPR, as shown in Fig. 13. For operational use, more stringent optical depth thresholds may be desired for such events, or the potential wet bias from using the

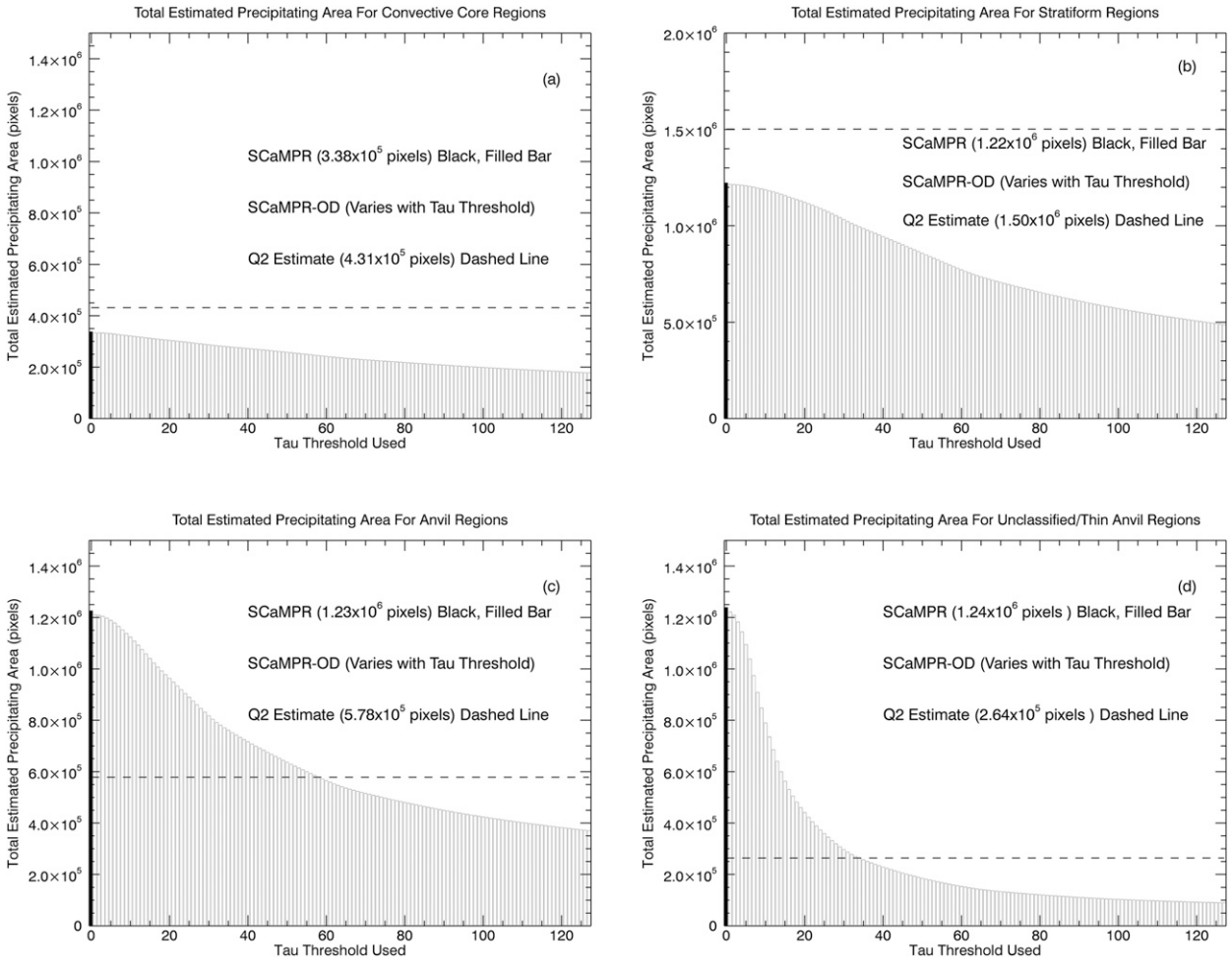

FIG. 7. Total estimated precipitating areas for (a) CC, (b) SR, (c) AC, and (d) thin anvil/unclassified regions from SCaMPR (black, filled bar), SCaMPR-OD (empty bars), and Q2 (dashed line) over the SGP region.

long-term skill-maximizing optical depth threshold of 22 should be taken into account.

Skill scores (CSI and HSS) for only the anvil regions also showed that SCaMPR-OD produced improvements over the original SCaMPR. However, these improvements were confined to a narrower range of optical depth thresholds, and the maximum performance in anvil regions was attained with lower optical depth thresholds than the overall skill-maximizing optical depth thresholds. This result is expected, as

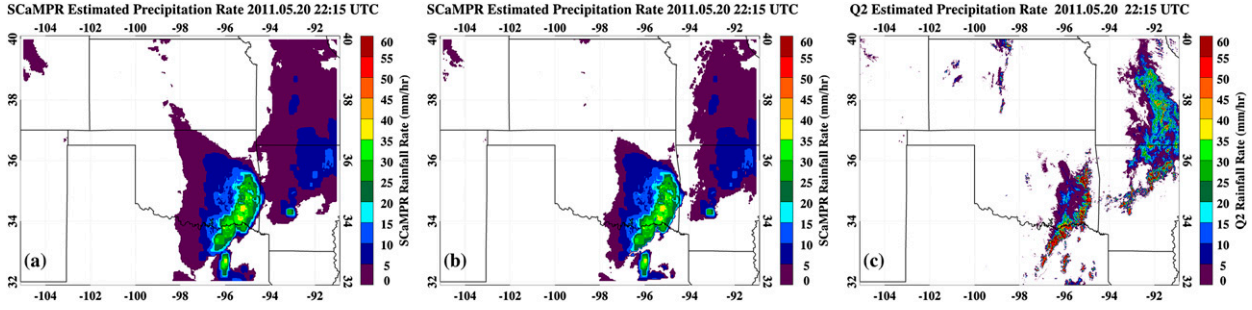

FIG. 8. Instantaneous precipitation rate estimates from (a) SCaMPR, (b) SCaMPR-OD, and (c) Q2 over the SGP region at 2215 UTC 20 May 2011.

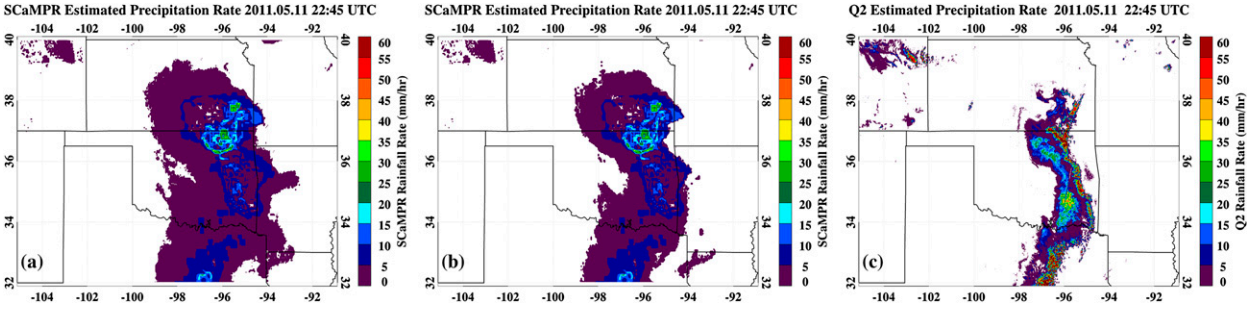

FIG. 9. As in Fig. 8, but for 2245 UTC 11 May 2011.

confining the analysis to only anvil regions significantly reduces the total number of hits and therefore the numerator in the skill score calculations. With this reduced numerator, the simultaneous loss of hits while the false alarm rate is decreased becomes significant more quickly, leading to a lower optical depth threshold that maximizes skill. When evaluating SCaMPR and SCaMPR-OD over all regions, more hits and false alarms can be trimmed off in anvil regions before skill is maximized because of the high number of hits in CC and SR regions (which are not reduced as significantly with application of the rain mask).

Since anvil precipitation is very light, and not the primary concern for operational use of products such as SCaMPR, the skill-maximizing threshold for the overall product is more important than the skill in these anvil regions. However, it is important to check that SCaMPR-OD does indeed improve skill here as well and that gains in overall skill are not simply from indiscriminately reducing estimated anvil precipitation. While skill scores for anvil regions are lower than the overall skill scores, which is expected from the greater uncertainties in both observing and estimating this lighter precipitation, they are still improved in SCaMPR-OD compared to SCaMPR. This improvement indicates that using an optical-depth-based rain mask provides a method to more accurately identify and estimate this lighter precipitation that often has a weaker relationship to BTs than CC and SR precipitation have.

While the estimated precipitating area from SCaMPR with the CSI-maximizing rain mask produces a total precipitating area similar to Q2, the total estimated precipitation volume exceeds Q2 by 42.99%. The mean rain rates from SCaMPR, SCaMPR-OD, and Q2 in CC, SR, AC, and unclassified regions of DCSs are given in Table 1. For SR regions, both original SCaMPR and SCaMPR-OD estimates produce mean precipitation rates of 6.73 and 6.90 mm h^{-1}, about 3 times as large as the Q2 mean SR precipitation rate (2.51 mm h^{-1}). These overestimates of mean precipitation rate also exist for the anvil (6.81 and 7.45 mm h^{-1}) and thin anvil/unclassified (4.19 and 5.00 mm h^{-1}) regions where the Q2 mean rates are only 1.18 and 1.19 mm h^{-1}, respectively (Table 1). As would be expected for an IR satellite-based precipitation retrieval algorithm, the mean precipitation rates in CC regions for SCaMPR (10.36 mm h^{-1}) and SCaMPR-OD (10.70 mm h^{-1}) are less than the Q2 (21.11 mm h^{-1}) mean CC rainfall rate (Table 1). It is important to note that the only adjustment to SCaMPR precipitation rates by the rain mask is setting rates to zero for pixels determined to be nonprecipitating, which implies that in all four classes the pixels that are filtered out by the mask tend to be on the low end of the rain-rate distribution.

The improvements brought to SCaMPR from the optical-depth-based rain mask could easily be applied to other IR-based satellite QPEs. As long as optical depth retrievals are available at the times when a satellite QPE provides an instantaneous rain-rate estimate, application of an optical-depth-based rain mask could aid in reducing the overestimates commonly noted during convection over anvil regions. However, a similar

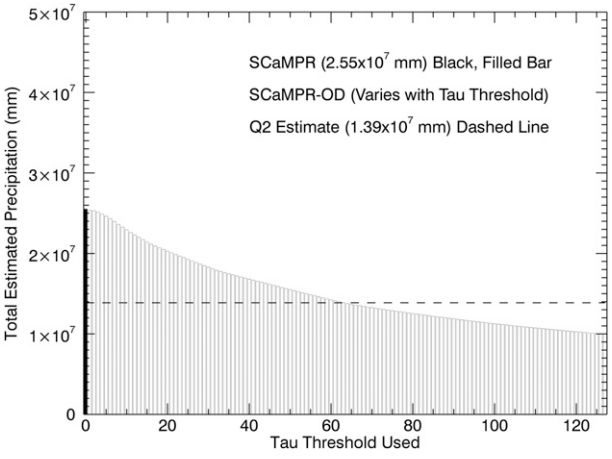

FIG. 10. Total estimated precipitation from SCaMPR (black, filled bar), SCaMPR-OD (empty bars), and Q2 (dashed lines) over the SGP region.

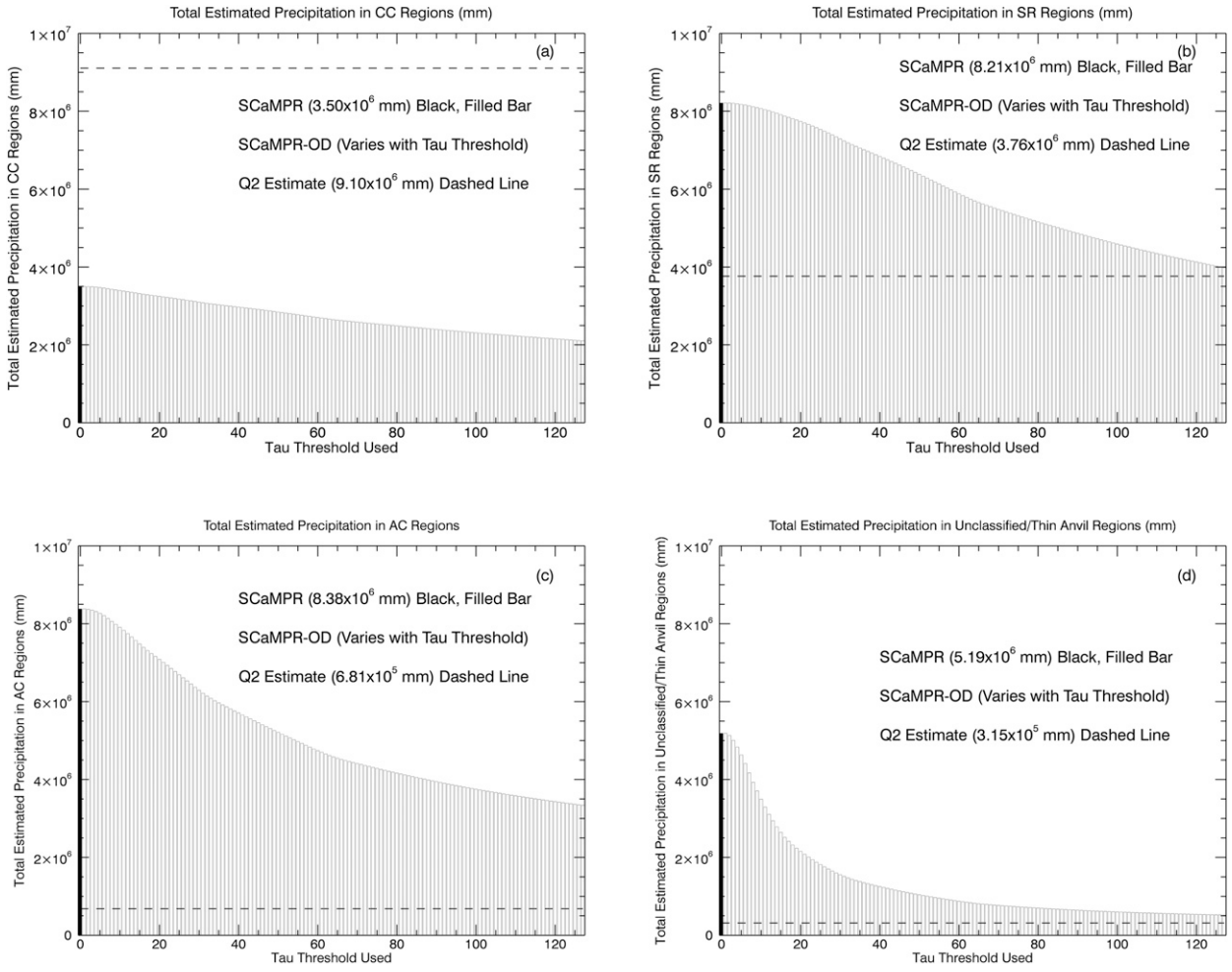

FIG. 11. Total estimated precipitation for (a) CC, (b) SR, (c) AC, and (d) thin anvil/unclassified regions from SCaMPR (black, filled bar), SCaMPR-OD (empty bars), and Q2 (dashed lines) over the SGP region.

analysis should be performed on any QPEs that apply this optical-depth-based rain mask as the biases and improvements in performance will likely differ, and the CSI-maximizing optical depth threshold value may also change depending on the satellite QPE it is applied to.

Uncertainties with this analysis must also be discussed, particularly those responsible for the unintuitive result of estimates of precipitation in CC and SR regions being reduced even at relatively low optical depth threshold levels. First, during the matching to a common grid, it is possible that slight shifting of the datasets may be responsible for some CC and SR regions being erroneously paired with lower optical depth values. However, this mismatch should be at a scale of less than one grid box and is not the sole source of uncertainty. Additionally, during the averaging process for Q2 and hybrid classification output, uncertainties exist. For example, the radar-identified CC, SR, and AC regions are identified at a 1 km × 1 km resolution and are paired with Q2 rain-rate estimates at a 1 km × 1 km resolution. However, averaging to the 4 km × 4 km grid to allow comparisons with the GOES and SCaMPR data requires taking the average Q2 over 16 grid boxes and the most frequent DCS region classification over these 16 grid boxes. As a result, it is possible that a 4 km × 4 km CC grid box may actually contain Q2 from AC regions, and with slight shifting could be matched with optical depth retrievals from AC regions. Conversely, a 4 km × 4 km AC grid box may have its Q2 rain rate influenced by CC and SR regions and may be paired with more optically thick clouds than expected. With the combination of shifting and averaging to the 4 km × 4 km grid, it is possible that a mismatch on the scale of an entire grid box may occur, which especially for isolated convection can be significant at times.

Further evidence of this potential uncertainty is evident in the rain mask filtering out the low end of the

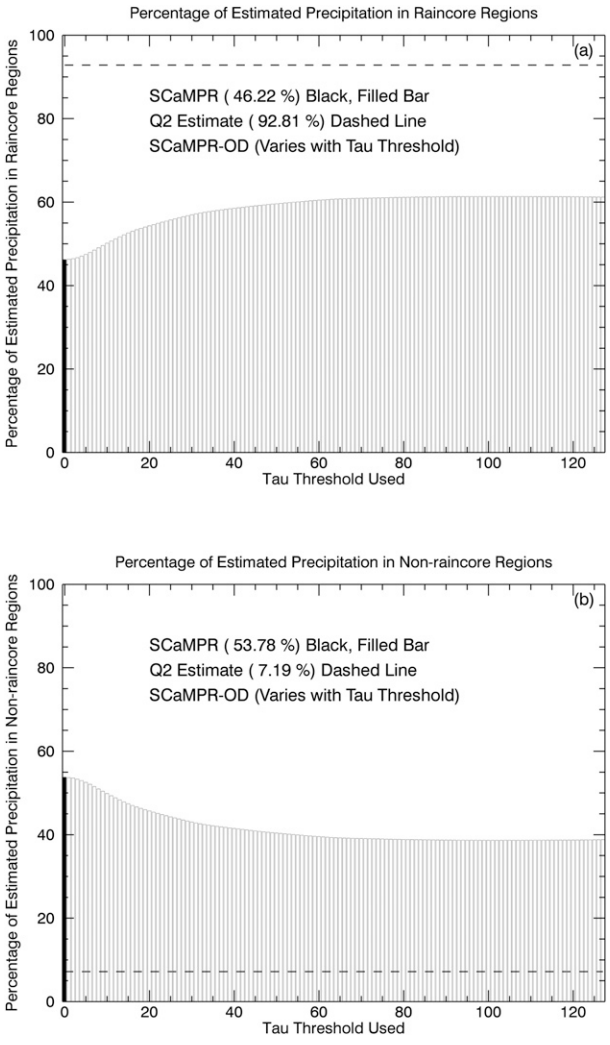

FIG. 12. Percentages of estimated precipitation in (a) rain-core (CC + SR) and (b) non-rain-core (AC + thin anvil/unclassified) regions from SCaMPR (black, filled bar), SCaMPR-OD (empty bars), and Q2 (dashed line) over the SGP region.

precipitation distribution for all DCS regions. The CC and SR regions that would not typically be expected to be filtered out based on optical depth are primarily those pixels that border AC regions and as a result have the lowest Q2 rainfall rates because of the averaging to a 4 km × 4 km grid. For AC regions, the more intense estimated rain rates are associated with those pixels being influenced by CC and SR regions, which are therefore more optically thick and more likely to not be filtered out by the rain mask. Last, there is great natural variability between optical depth and rainfall rate. While optical depth and rainfall rate are correlated (Kühnlein et al. 2010), optically thick clouds may produce no rainfall while optically thin clouds do produce rainfall. This natural variability is also responsible for instances where actual precipitation can be filtered out even at relatively low optical depth values; however, it is still very unlikely for optically thin clouds to be producing precipitation. Although the relationship between optical depth and precipitating area is robust and improves the skill of SCaMPR, natural variability does produce some nonnegligible uncertainty.

For this study, evaluation of the optical-depth-based rain mask was only performed during daylight hours because of the limitations of the optical depth retrieval algorithms. Without visible measurements from the GOES data during nighttime, accurate retrievals of optical depth greatly increase in difficulty. At the time of this study, an algorithm still in development by the Minnis group at NASA Langley Research Center for nighttime optical depth retrievals from GOES data did qualitatively show potential for reducing SCaMPR anvil precipitation overestimates at night. However, it is too early to develop a nighttime rain mask using GOES-retrieved nighttime optical depth because of their large uncertainties. As the majority of precipitation associated with DCSs over the contiguous United States occurs during nighttime, future improvements in optical depth retrievals from GOES data have the potential of further improving satellite QPEs. Currently, optical depth retrievals from polar-orbiting satellites at night would be sufficient to improve satellite QPEs in a way similar to that shown in this study for those that provide information such as the Visible Infrared Imaging Radiometer Suite (VIIRS) Day/Night Band (DNB; Lee et al. 2006). Looking forward, it is possible that the additional bands on the GOES-R Advanced Baseline Imager (ABI; http://www.goes-r.gov/spacesegment/abi.html) will improve nighttime optical depth retrievals sufficiently for optical-depth-based rain masks to provide consistent, significant improvements in the skill of satellite QPEs at night.

6. Conclusions

Application of an optical-depth-based rain mask to SCaMPR improved the performance of SCaMPR in multiple ways. First, the CSI for detection of precipitation from SCaMPR-OD with the optimal τ threshold of 22 was increased to 0.39 from 0.34 from the original SCaMPR. Additionally, improvements in CSI and HSS were made over the original version of SCaMPR for a broad range of rain mask optical threshold values (1–50). Similar improvements were seen using the HSS as a metric to evaluate performance. Examination of only anvil and thin anvil/unclassified regions also showed improvements in skill (CSI and HSS) in SCaMPR-OD compared to the

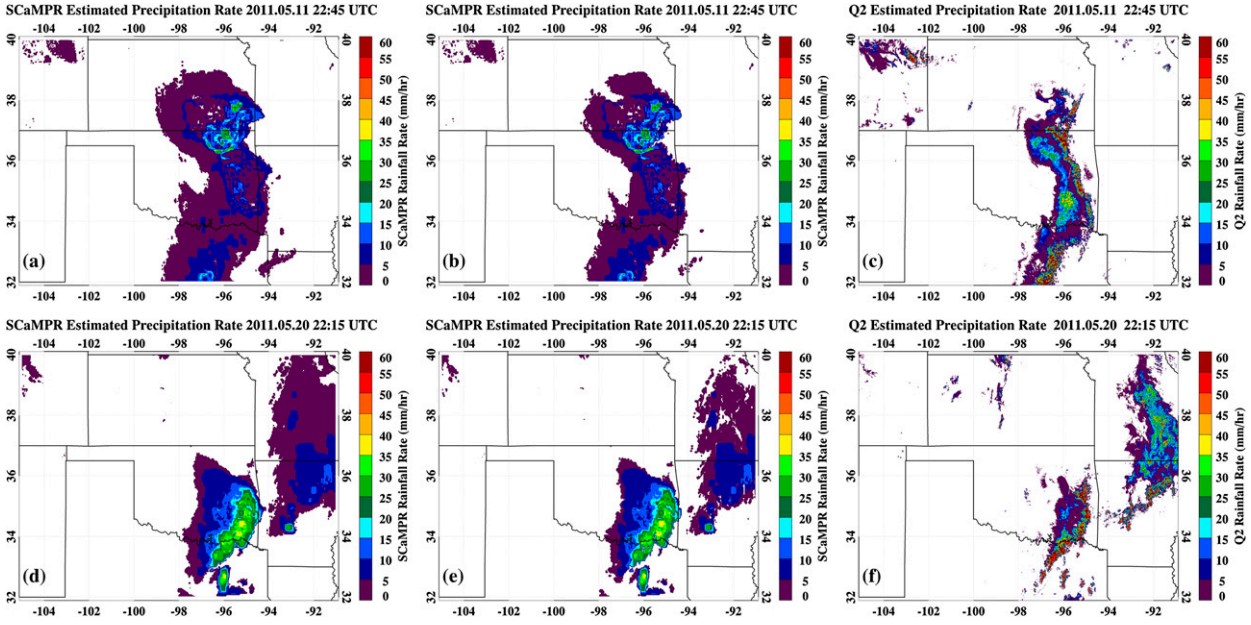

FIG. 13. Instantaneous precipitation rate estimates for (a),(d) SCaMPR-OD; (b),(e) SCaMPR-OD with a rain mask using an optical depth threshold of 40; and (c),(f) Q2 at (top) 2245 UTC 11 May and (bottom) 2215 UTC 20 May 2011.

original SCaMPR. Total estimated precipitating area also closely matched the Q2 precipitating area when the skill-maximizing rain mask was applied, correcting the large overestimates in precipitating area of the original SCaMPR.

Even with the CSI-maximizing rain mask applied, the total estimated precipitation of SCaMPR still produced large overestimates compared to Q2 (which also have a wet bias). While this wet bias was significantly reduced after application of the rain mask, the tendency for SCaMPR to have significantly higher retrieved rain rates in anvil and stratiform regions (which comprise the majority of the area of a DCS) compared to what is observed produce overestimates even when a reasonable precipitating area has been retrieved. This bias is most apparent in the analysis of rain-core versus non-rain-core precipitation, where the majority of estimated precipitation from SCaMPR falls in non-rain-core regions, compared to only ~7% for Q2. Application of the rain masks to SCaMPR improves this distribution of precipitation, but SCaMPR with the rain mask applied still have a significant dry bias in rain cores and a significant wet bias in non-rain-core regions.

The problems that SCaMPR IR-based precipitation retrievals have are not unique; therefore, other satellite QPEs could also be improved with the application of an optical-depth-based rain mask. More general application of this rain mask could be applied to satellite QPEs from both geostationary and polar-orbiting satellites, but limitations in nighttime optical depth retrievals are the current major limitation of this rain mask. However, as retrieval algorithms continue to improve, and with additional information expected to be available after the launch of GOES-R, it is highly possible that nighttime optical-depth-based rain masks will eventually provide consistent and significant improvements in the skill of satellite QPEs just as this daytime rain mask currently does. Additionally, future work could be done to explore the potential of using retrieved optical depth to adjust rain rates for SCaMPR to address the bias in estimated rain rates by DCS region identified in this study. As the largest optical depth values are often associated

TABLE 1. Mean precipitation rates for each DCS region for Q2, SCaMPR, and SCaMPR-OD.

DCS region	Mean rain rate (Q2) (mm h^{-1})	Mean rain rate (SCaMPR) (mm h^{-1})	Mean rain rate (SCaMPR-OD) (mm h^{-1})
CC	21.11	10.36	10.70
SR	2.51	6.73	6.90
AC	1.18	6.81	7.45
Thin anvil/unclassified	1.19	4.19	5.00

with the most intense rain rates for a DCS, it appears possible that optical depth could be used as a predictor for rain rates in addition to its use as a rain mask.

Acknowledgments. The Q2 product was obtained from the NOAA/National Severe Storms Laboratory. This research was primarily supported by NOAA GOES-R project with Award Number NA11NES440004 at the University of North Dakota. The University of North Dakota authors were also supported by the U.S. Department of Energy Atmospheric Systems Research project with Award Number DE-SC0008468. Dr. Zhe Feng developed the hybrid classification scheme used in this study. He was supported by the U.S. Department of Energy, Office of Science, Biological and Environmental Research as part of the Regional and Global Climate Modeling Program and Atmospheric System Research program. The contents of this paper are solely the opinions of the authors and do not constitute a statement of policy, decision, or position on behalf of NOAA or the U.S. Government.

REFERENCES

Adler, F. R., and A. J. Negri, 1988: A satellite infrared technique to estimate tropical convective and stratiform rainfall. *J. Appl. Meteor.*, **27**, 30–51, doi:10.1175/1520-0450(1988)027<0030:ASITTE>2.0.CO;2.

Amitai, E., W. Petersen, X. Llort, and S. Vasiloff, 2012: Multiplatform comparisons of rain intensity for extreme precipitation events. *IEEE Trans. Geosci. Remote Sens.*, **50**, 675–686, doi:10.1109/TGRS.2011.2162737.

Chen, S., and Coauthors, 2013: Evaluation and uncertainty estimation of NOAA/NSSL next-generation National Mosaic Quantitative Precipitation Estimation Product (Q2) over the continental United States. *J. Hydrometeor.*, **14**, 1308–1322, doi:10.1175/JHM-D-12-0150.1.

Feng, Z., X. Dong, B. Xi, C. Schumacher, P. Minnis, and M. Khaiyer, 2011: Top-of-atmosphere radiation budget of convective core/stratiform rain and anvil clouds from deep convective systems. *J. Geophys. Res.*, **116**, D23202, doi:10.1029/2011JD016451.

——, ——, ——, S. McFarlane, A. Kennedy, B. Lin, and P. Minnis, 2012: Life cycle of deep convective systems in a Lagrangian framework. *J. Geophys. Res.*, **117**, D23201, doi:10.1029/2012JD018362.

Hong, Y., R. F. Adler, A. Negri, and G. J. Huffman, 2007: Flood and landslide applications of near real-time satellite rainfall products. *Nat. Hazards*, **43**, 285–294, doi:10.1007/s11069-006-9106-x.

Kirstetter, P.-E., and Coauthors, 2012: Toward a framework for systematic error modeling of spaceborne precipitation radar with NOAA/NSSL ground radar–based National Mosaic QPE. *J. Hydrometeor.*, **13**, 1285–1300, doi:10.1175/JHM-D-11-0139.1.

Krajewski, W., and J. Smith, 2002: Radar hydrology: Rainfall estimation. *Adv. Water Resour.*, **25**, 1387–1394, doi:10.1016/S0309-1708(02)00062-3.

Kühnlein, M., B. Thies, T. Nauß, and J. Bendix, 2010: Rainfall-rate assignment using MSG SEVIRI data—A promising approach to spaceborne rainfall-rate retrieval for midlatitudes. *J. Appl. Meteor. Climatol.*, **49**, 1477–1495, doi:10.1175/2010JAMC2284.1.

Kuligowski, R. J., 2010: GOES-R Advanced Baseline Imager (ABI) algorithm theoretical basis document for rainfall rate (QPE). Algorithm Theoretical Basis Doc., NOAA/NESDIS, 44 pp. [Available online at http://www.goes-r.gov/products/ATBDs/baseline/Hydro_RRQPE_v2.0_no_color.pdf.]

Lee, T. E., S. D. Miller, F. J. Turk, C. Schueler, R. Julian, S. Deyo, P. Dills, and S. Wang, 2006: The NPOESS VIIRS day/night visible sensor. *Bull. Amer. Meteor. Soc.*, **87**, 191–199, doi:10.1175/BAMS-87-2-191.

Maddox, R., J. Zhang, J. Gourley, and K. Howard, 2002: Weather radar coverage over the contiguous United States. *Wea. Forecasting*, **17**, 927–934, doi:10.1175/1520-0434(2002)017<0927:WRCOTC>2.0.CO;2.

Minnis, P., and Coauthors, 2008: Near-real time cloud retrievals from operational and research meteorological satellites. *Remote Sensing of Clouds and the Atmosphere XIII*, R. H. Picard et al., Eds., International Society for Optical Engineering (SPIE Proceedings, Vol. 7107), 710703, doi:10.1117/12.800344.

Negri, A. J., and R. F. Adler, 1981: Relationship of satellite-based thunderstorm intensity to radar-estimated rainfall. *J. Appl. Meteor.*, **20**, 288–300, doi:10.1175/1520-0450(1981)020<0288:ROSBTI>2.0.CO;2.

Scofield, R. A., and R. J. Kuligowski, 2003: Status and outlook of operational satellite precipitation algorithms for extreme-precipitation events. *Wea. Forecasting*, **18**, 1037–1051, doi:10.1175/1520-0434(2003)018<1037:SAOOOS>2.0.CO;2.

Steiner, M., R. A. Houze, and S. E. Yuter, 1995: Climatological characterization of three-dimensional storm structure from operational radar and rain gauge data. *J. Appl. Meteor.*, **34**, 1978–2007, doi:10.1175/1520-0450(1995)034<1978:CCOTDS>2.0.CO;2.

Stenz, R., X. Dong, B. Xi, and R. J. Kuligowski, 2014: Assessment of SCaMPR and NEXRAD Q2 precipitation estimates using Oklahoma Mesonet observations. *J. Hydrometeor.*, **15**, 2484–2500, doi:10.1175/JHM-D-13-0199.1.

Vicente, G. A., R. A. Scofield, and W. P. Menzel, 1998: The operational GOES infrared rainfall estimation technique. *Bull. Amer. Meteor. Soc.*, **79**, 1883–1898, doi:10.1175/1520-0477(1998)079<1883:TOGIRE>2.0.CO;2.

Wu, W., D. Kitzmiller, and S. Wu, 2012: Evaluation of radar precipitation estimates from the National Mosaic and Multisensor Quantitative Precipitation Estimation System and the WSR-88D precipitation processing system over the conterminous United States. *J. Hydrometeor.*, **13**, 1080–1093, doi:10.1175/JHM-D-11-064.1.

Zhang, J., and Y. Qi, 2010: A real-time algorithm for the correction of brightband effects in radar-derived precipitation estimation. *J. Hydrometeor.*, **11**, 1157–1171, doi:10.1175/2010JHM1201.1.

——, and Coauthors, 2011: National Mosaic and Multi-Sensor (NMQ) System: Description, results, and future plans. *Bull. Amer. Meteor. Soc.*, **92**, 1321–1338, doi:10.1175/2011BAMS-D-11-00047.1.

——, and Coauthors, 2014: Initial operating capabilities of quantitative precipitation estimation in the multi-radar multi-sensor system. *28th Conf. on Hydrology*, Atlanta, GA, Amer. Meteor. Soc., JP5.3. [Available online at https://ams.confex.com/ams/94Annual/webprogram/Paper240487.html.]